Design and Control of a Compact Lightweight Planar Positioner Moving Over a Concentrated-Field Magnet Matrix

Vu Huy Nguyen, *Student Member, IEEE*, and Won-jong Kim, *Senior Member, IEEE*

***Abstract*—In this paper, a single-moving-part planar positioner with six coils is designed and implemented. A concentrated-field permanent-magnet matrix is employed as the stationary part. The moving platen has a compact size (185.4 mm × 157.9 mm), light mass (0.64 kg) and low-center-of-gravity. The moving platen carries three planar-motor armatures with two phases per motor. Force calculation is based on the Lorentz force law and conducted by volume integration. In order to deal with the nonlinearity due to trigonometric dependencies in the force-current relation, modified proportional-integral-derivative (PID) and lead-and-PI compensators are designed with computed currents to close the control loop and obtain the desired performances. Experimental results verified the commutation law and the force calculation. The new design with only six coils allows for simplification of the control algorithm and reduced power consumption of the positioner. The maximum travel ranges in x, y, and the rotation about the vertical axis are 15.24 cm, 20.32 cm, and 12.03°, respectively. The positioning resolution in x and y is 8 μm with the rms position noise of 6 μm. The positioning resolution in rotations about the vertical axis is 100 μrad.**

***Index Terms*—Concentrated-field magnet matrix, multiaxis positioner, permanent-magnet actuator, precision planar positioner.**

I. Introduction

PRECISION positioners are employed in many important industrial applications. Among them are wafer steppers in photolithography, scanning microscopes, and surface profilometers. Planar positioners with high precision are broadly used in microscale alignment and assembly. In microelectronic assembly, they are key instruments for the placement and transportation of electronic components.

Conventional x–y positioners are complicated multimoving-part mechanical systems, in which a gantry and a crossed-axis stage are the two typical structures, and rotary electric motors with lead/ball screws are commonly used. The mechanical joints in the multiple moving parts slow down the response and reduce the mechanical rigidity of the positioner's structure. Friction in mechanical transmissions and between the moving parts of the positioners decreases their position accuracy and reduces the durability of the mechanisms. Friction limits the speed and should be avoided in positioning systems with ultrahigh speed or precise motions. These can be overcome by designing a single-moving-part positioner with air or magnetic bearings to support the moving platen against gravity, allowing for smooth high-speed motions without energy loss and damage due to friction. In addition, compared to the multimoving-part positioners, single-moving-part ones are simpler to be modeled for dynamic analysis and control.

The Sawyer motor, with long travel ranges, high speed, and open-loop-positioning capability, was introduced in [1]. However, many protrusions in the Sawyer motor stator generate significant cogging force. Kim developed a high-precision planar magnetic-levitation stage [2], in which, there were four 3-phase motors with 11 windings per phase and each motor could generate two independent force components. The linear current-force relation was derived by the *DQ* decomposition and was position independent. A surface induction motor for 2-D drive was developed by Fujii and Kihara [3]. In their design, there were armature windings arranged symmetrically in the primary part, which had the round shape, and a flat conducting plate attached to a back-iron plate in the secondary part. Cho *et al*. designed a 2-D permanent-magnet array for planar motors [4] and developed a permanent-magnet synchronous planar motor [5]. The moving part had four 3-phase forcers; each generated the force in either x or y. Hu developed an advanced-technology-program stage [6] that employed a superimposed concentrated-field Halbach magnet matrix in the stationary part and three 3-phase motors arranged in a triangle configuration, each with four windings. Yu and Kim developed a compact six-axis precision positioner [7], also employing a superimposed concentrated-field magnet matrix and three 3-phase motors. Choi and Gweon constructed a dual-servo stage using Halbach linear active magnetic bearings [8]. The design mainly comprised a coarse stage, which was driven by an *H*-structure with three linear motors, a fine stage with four Halbach linear active magnetic bearings controlling the out-of-plane motions, and four voice coil motors controlling the in-plane motions. Ro and Park introduced a 3-DOF compact ultraprecision planar stage using four single-phase linear motors with coils and iron cores in the stationary part [9]. Khan *et al*. introduced a long stroke electromagnetic xy positioning stage [10].

This paper presents the design, construction, and control of a moving-coil single-moving-part planar positioner that employs

Manuscript received March 17, 2011; revised August 1, 2011 and November 1, 2011; accepted March 27, 2012. Date of publication May 14, 2012; date of current version January 18, 2013. Recommended by Technical Editor G. Yang.

V. H. Nguyen was with Texas A&M University, College Station, TX 77843-3123 USA. He is now with the University of Transport and Communications, Hanoi 10000, Vietnam (e-mail: huyvu1182@gmail.com).

W.-J. Kim is with Texas A&M University, College Station, TX 77843-3123 USA (e-mail: wjkim@tamu.edu).

Color versions of one or more of the figures in this paper are available online at http://ieeexplore.ieee.org.

Digital Object Identifier 10.1109/TMECH.2012.2196052

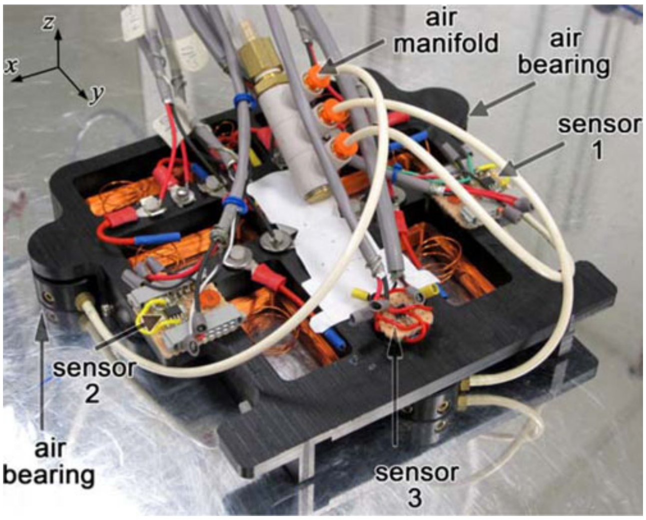

Fig. 1. Photograph of the compact planar positioner.

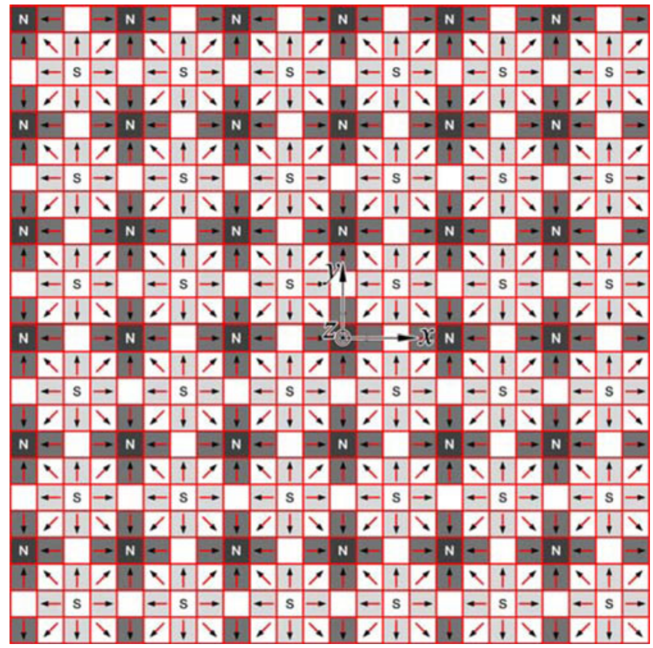

Fig. 2. Illustration of the superimposed concentrated-field magnet matrix.

a superimposed concentrated-field magnet matrix [2], [11]. The first key contribution of the design presented in this paper is that a novel electromagnetic commutation with a linear current-force transformation has been proposed and tested. The second key contribution is the minimized number of coils (only six compared to 24 in [3], 12 in [5], and 9 in [7]) assembled in a single-tool-cutting frame. The linear current–force relation and the reduced number of coils simplify the control strategy of the positioner and facilitate real-time implementation of the controllers. For translational motions in the xy plane, the achieved acceleration is $3.75\,\mathrm{m/s^2}$ compared to $3.6\,\mathrm{m/s^2}$ in [7] while the coil volume is 43% and the coil resistance is 40% of those in [7], respectively. The compact-size low-center-of-gravity moving platen has the height of only 22.2 mm compared to 31 mm in [9], being suitable for applications that require minimum height of the x–y positioners. Fig. 1 shows a photograph of the fully assembled positioner over a mirror-finished aluminum plate on top of the magnet matrix.

This paper is organized as follows. The electromagnetic design of the positioner is discussed in Section II. The mechanical design is presented in Section III. Section IV describes the hardware and instrumentation system. Section V discusses the control system design. Experimental results are provided in Section VI to verify the working principle and the force calculation of the positioner. Our conclusions are given in Section VII.

II. Electromagnetic Design

A. *Superimposed Concentrated-Field Magnet Matrix*

Two single-axis Halbach magnet arrays [12] are orthogonally superimposed into a plane to produce a concentrated-field magnet matrix [2], [11], [13]. The x-axis magnet array generates only the x-direction and the z-direction magnetic flux-density components. The y-axis magnet array generates only the y-direction and the z-direction magnetic flux-density components. In the superimposed magnet matrix, the resultant magnetization vector of a magnet block is the sum of two corresponding magnetization vectors, one in the x- or z-direction from the x-axis magnet array, and one in the y- or z-direction from the y-axis magnet array. Therefore, different resultant magnetization vectors are formed as in Fig. 2, where the arrangement of the magnet blocks in such a magnet matrix with six spatial periods each side is illustrated. In Fig. 2, the magnet blocks noted by N or S have the magnetization vectors in the positive or negative z-direction, respectively. The magnet blocks with the arrows parallel to x or y and pointing to the N have the magnetization vectors directed 45° with respect to the positive z-axis. The magnet blocks with the arrows parallel to x or y and pointing away from the S have the magnetization vectors directed 135° with respect to the positive z-axis. The magnet blocks with the arrows directed 45° with respect to x or y have the magnetization vectors in a horizontal plane parallel to the xy plane. The blank squares in Fig. 2 are nonmagnetic aluminum spacers. The magnet blocks noted as N or S are NdFeB50 with the remanence of 1.43 T. All the magnet blocks noted with an arrow are NdFeB30 with the remanence of 1.10 T. One spatial pitch of the magnet matrix along the x- or y-axis is $L = 50.8$ mm, corresponding to four magnet blocks. The plane of $z = 0$ is the top plane of the magnet matrix.

With linear superposition applied, the resultant magnetic flux density everywhere above the top surface of the magnet matrix is the vector sum of the magnetic flux densities generated by the two single-axis magnet arrays. The complete development of the field solutions for the superimposed concentrated-field magnet matrix was presented in [2], [14]. The three components of the magnetic flux density are as follows:

$$B_x(x,z) = \sum_{k=0}^{+\infty} (-1)^{k+1} \frac{2\sqrt{2}\mu_0 M_0}{\pi n} \times (1 - e^{-\gamma_n \Delta}) e^{-\gamma_n z} \sin(\gamma_n x) \qquad (1)$$

$$B_y(y,z) = \sum_{k=0}^{+\infty} (-1)^{k+1} \frac{2\sqrt{2}\mu_0 M_0}{\pi n} \times (1 - e^{-\gamma_n \Delta}) e^{-\gamma_n z} \sin(\gamma_n y) \tag{2}$$

$$B_{z1}(x,z) = \sum_{k=0}^{+\infty} (-1)^{k} \frac{2\sqrt{2}\mu_0 M_0}{\pi n} \times (1 - e^{-\gamma_n \Delta}) e^{-\gamma_n z} \cos(\gamma_n x) \tag{3}$$

$$B_{z2}(y,z) = \sum_{k=0}^{+\infty} (-1)^{k} \frac{2\sqrt{2}\mu_0 M_0}{\pi n} \times (1 - e^{-\gamma_n \Delta}) e^{-\gamma_n z} \cos(\gamma_n y) \tag{4}$$

$$B_z(x,y,z) = B_{z1}(x,z) + B_{z2}(y,z). \tag{5}$$

Here, $n = 4k + 1$ and k is a nonnegative integer, μ_0 is the permeability of the free space, M_0 is the peak magnetization, $\mu_0 M_0 = 0.71$ T, $\Delta = 12.7$ mm, and $\gamma_n = 2\pi n/L$. $B_{z1}(x, z)$ and $B_{z2}(y, z)$ are the z-direction magnetic flux-density component, generated by the single x- and y-axes Halbach magnet arrays, respectively. $B_x(x, z)$, $B_y(y, z)$, and $B_z(x, y, z)$ are the resultant x-, y-, and z-direction magnetic flux-density components, respectively, generated by the superimposed magnet matrix. For the magnet matrix employed in the work presented in this paper, (1)–(5) are valid over an area of 30.5 cm $\times$ 30.5 cm.

B. Design of a Single Forcer and the Moving Platen

To drive the moving platen in 3 DOFs in the xy plane, three independent forcers are required. The arrangement of these three forcers carried on the bottom of the moving platen is shown in Fig. 3 (Coils 1 and 2, Coils 3 and 4, and Coils 5 and 6). Each forcer, on the horizontal plane, generates either f_x or f_y governed by the Lorentz force law, $\boldsymbol{F} = \boldsymbol{J} \times \boldsymbol{B}$, where $\boldsymbol{J}$ is the current density [A/m^2] flowing in the coil, $\boldsymbol{B}$ is the flux density [T] generated by the magnet matrix, and $\boldsymbol{F}$ is the force density [N/m^3] acting on the current-carrying coil. The force vector $\boldsymbol{f}$ [N] is the volume integral of $\boldsymbol{F}$ of the relevant coil volume.

Fig. 4 demonstrates the electromagnetic working principle that makes the most of the spatial periodicity of the flux-density solutions (1)–(5). Since B_z varies sinusoidally with the spatial period of L along the y-axis as in (3)–(5), two long sides (I and III in Fig. 5) of the coil were designed to have a separation of $L/2$. In Fig. 4(a), the y-direction forces acting on the two long sides have the same magnitudes and direction by the Lorentz force law regardless of the coil's location over the magnet matrix and the direction of the coil current. In order to always cancel out f_x, the separation between the two short coil sides (II and IV in Fig. 5) must be an integer multiple of L.

There are certain positions where the resultant f_y acting on the entire coil is zero regardless of the current. This takes place when the two long sides are located at an equal distance from a peak of B_z as shown in Fig. 4(b). In Fig. 4(c), a second coil is added with its long sides being placed at the positive and negative peaks of B_z. By doing this, at the position where the resultant f_y acting on the first coil is zero, f_y on the second coil

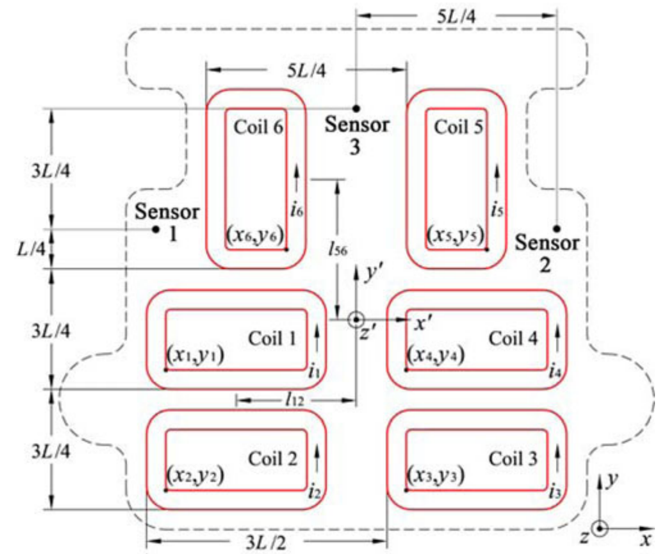

Fig. 3. Moving platen with three forcers, each with Coils 1 and 2, Coils 3 and 4, and Coils 5 and 6. Locations of the three Hall-effect sensors on the moving platen are given.

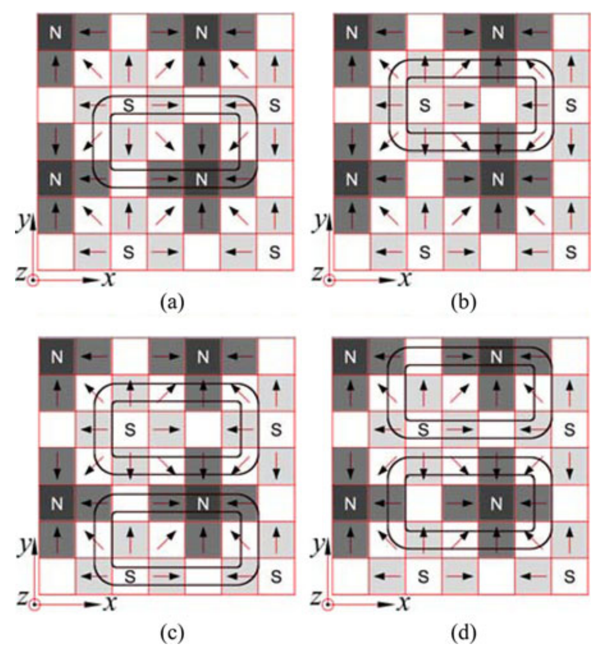

Fig. 4. Various positions of the coils over the magnet matrix.

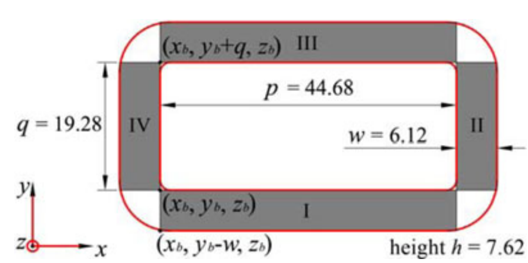

Fig. 5. Coil dimension, unit: mm.

is maximized. Fig. 4(d) shows another position of the two coils where f_y on the second coil is zero and f_y on the first coil is maximized. The set of two coils (Coils 1 and 2 or Coils 3 and 4) in this forcer being placed with a distance of $3L/4$ becomes a 2-phase planar motor armature with a 270° (or −90°) phase difference. For the symmetry of the moving platen, an air bearing is placed between Coils 5 and 6, which are then separated by 450° (or 90°). However, their working principle stays essentially the same as that of Coils 1 and 2.

The coil dimension is given in Fig. 5. AWG #24 heavy-build heat-bondable wire is used. The linear coil-turn densities λ along the width w and β along the height h of the coil are 1969 turns/m and 1712 turns/m, respectively. By our measurements, the coil resistance and inductance are 1.98 Ω and 1.28 mH, respectively. The mass of each coil is 0.043 kg.

C. Force Calculation and Current–Force Transformation

To calculate the force acting on a coil, a volume integration of the force density is performed [14]. First, the electromagnetic forces acting on the rectangular coil sides are calculated. The electromagnetic forces due to the nth-order harmonics in the Fourier series representations of $B_{z1}(x, z)$ and $B_{z2}(y, z)$ acting on Sides I and III in Fig. 5, are

$$f_{yn}^{I} = -\frac{i\lambda\beta L}{\pi n\gamma_n} B_n(z_b)\left\{w\cos\left[\gamma_n\left(x_b+\frac{p}{2}\right)\right]\sin\left(\frac{\gamma_n p}{2}\right) + p\cos\left[\gamma_n\left(y_b-\frac{w}{2}\right)\right]\sin\left(\frac{\gamma_n w}{2}\right)\right\}(1-e^{-\gamma_n h}) \quad (6)$$

$$f_{yn}^{III} = \frac{i\lambda\beta L}{\pi n\gamma_n} B_n(z_b)\left\{w\cos\left[\gamma_n\left(x_b+\frac{p}{2}\right)\right]\sin\left(\frac{\gamma_n p}{2}\right) + p\cos\left[\gamma_n\left(y_b+q+\frac{w}{2}\right)\right]\sin\left(\frac{\gamma_n w}{2}\right)\right\}(1-e^{-\gamma_n h}) \quad (7)$$

$$B_n(z_b) = (-1)^k \frac{2\sqrt{2}\mu_0 M_0}{\pi n}(1-e^{-\gamma_n \Delta})e^{-\gamma_n z_b} \quad (8)$$

where (x_b, y_b, z_b) is the base point of the coil to calculate the electromagnetic force by volume integration. The plane of $z = z_b$ contains the bottom surface of the coil.

When the coil moves along the y-axis, the force f_y corresponding to the nth-order harmonics of B_{z2} varies sinuisoidally with respect to y. The ratio between the amplitude of the force f_{y5} due to the fifth-order harmonics ($k = 1$, $n = 5$) and that of the force f_{y1} due to the fundamental harmonics ($k = 0$, $n = 1$) is calculated to be 0.950%. The ratio between the amplitude of the force f_{y9} due to the ninth-order harmonics and that of the force f_{y1} is only 0.010%. Therefore, to save time for real-time computation, only the fundamental harmonics of B_z is used to calculate the f_x and f_y acting on the moving platen. With $n = 1$, $k = 0$, $q + w = L/2$, $\gamma_1 = 2\pi/L$, and the first term in the right side of (6) and that of (7) canceling out, the y-direction forces in (6) and (7) are summed to yield the resultant force f_y acting on the coil with the current i flowing in it

$$\begin{aligned} f_y &= -\frac{2i\lambda\beta L}{\pi\gamma_1} B_1(z_b) p\cos\left[\gamma_1\left(y_b-\frac{w}{2}\right)\right] \times \sin\left(\frac{\gamma_1 w}{2}\right)(1-e^{-\gamma_1 h}) \\ &= -\frac{4i\lambda\beta p}{\gamma_1^2} B_1(z_b)\sin\left(\frac{\gamma_1 w}{2}\right)(1-e^{-\gamma_1 h}) \times \cos\left[\gamma_1\left(y_b-\frac{w}{2}\right)\right]. \end{aligned} \quad (9)$$

Two y-direction forces acting on Sides I and III due to B_{z1} generated by the x-axis magnet array cancel out, as seen in (6), (7) and illustrated in Fig. 4. Two y-direction forces acting on Sides I and III due to B_{z2} generated by the y-axis magnet array contribute to the resultant force in (9). Projected on the horizontal xy plane, the y-direction forces acting on Sides I and III due to B_{z2} have the acting points in the symmetrical axis of the coil parallel to the y-axis. Therefore, $l_{12} = 38.1$ mm in Fig. 3 is used to calculate the torque about the vertical axis generated by the y-direction forces acting on Coils 1 and 2. Similarly, $l_{56} = 44.4$ mm is to calculate the torque acting on the platen, being generated by the x-direction forces acting on Coils 5 and 6. The positions in z of all the base points of the six coils are $z_1 = 3$ mm.

From (9), with the currents i_1 and i_2 flowing in the coils and the base points of (x_1, y_1, z_1) and (x_2, y_2, z_1) to perform volume integration, and $y_2 = y_1 - 3L/4$, the y-direction electromagnetic forces acting on Coils 1 and 2 are, respectively,

$$f_{y,1} = -b_0 i_1 \cos\left[\gamma_1\left(y_1-\frac{w}{2}\right)\right] \quad (10)$$

$$f_{y,2} = -b_0 i_2 \cos\left[\gamma_1\left(y_2-\frac{w}{2}\right)\right] = b_0 i_2 \sin\left[\gamma_1\left(y_1-\frac{w}{2}\right)\right] \quad (11)$$

where

$$b_0 = \frac{4\lambda\beta p}{\gamma_1^2} B_1(z_1)\sin\left(\frac{\gamma_1 w}{2}\right)(1-e^{-\gamma_1 h}). \quad (12)$$

The y-direction resultant force acting on Coils 1 and 2 is

$$f_{y,12} = b_0\left\{-i_1\cos\left[\gamma_1\left(y_1-\frac{w}{2}\right)\right] + i_2\sin\left[\gamma_1\left(y_1-\frac{w}{2}\right)\right]\right\}. \quad (13)$$

The y-direction resultant force acting on Coils 3 and 4 is

$$f_{y,34} = b_0\left\{-i_4\cos\left[\gamma_1\left(y_1-\frac{w}{2}\right)\right] + i_3\sin\left[\gamma_1\left(y_1-\frac{w}{2}\right)\right]\right\}. \quad (14)$$

For the x-direction electromagnetic forces acting on Coils 5 and 6, (9) must be applied to these coils with the base points of $(y_5, -x_5, z_1)$ and $(y_6, -x_6, z_1)$, respectively, in the $(y, -x, z)$ frame. Note that $x_5 = x_6 + 5L/4$, as seen in Fig. 3

$$f_{x,5} = -b_0 i_5 \cos\left[\gamma_1\left(-x_5 - \frac{w}{2}\right)\right]$$
$$= b_0 i_5 \sin\left[\gamma_1\left(x_6 + \frac{w}{2}\right)\right] \tag{15}$$
$$f_{x,6} = -b_0 i_6 \cos\left[\gamma_1(-x_6 - \frac{w}{2})\right]$$
$$= -b_0 i_6 \cos\left[\gamma_1\left(x_6 + \frac{w}{2}\right)\right]. \tag{16}$$

The x-direction resultant force acting on Coils 5 and 6 is

$$f_{x,56} = b_0\left\{-i_6 \cos\left[\gamma_1\left(x_6 + \frac{w}{2}\right)\right] + i_5 \sin\left[\gamma_1\left(x_6 + \frac{w}{2}\right)\right]\right\}. \tag{17}$$

The resultant torque acting on the platen about the vertical axis is

$$T_{x,p} = -f_{y,12} l_{12} + f_{y,34} l_{12} - f_{x,56} l_{56}. \tag{18}$$

The current–force transformation for the six-coil moving platen is derived to be

$$\boldsymbol{f} = \boldsymbol{A}\boldsymbol{i} \tag{19}$$

$$\boldsymbol{A} = \begin{bmatrix} 0 & 0 & 0 & 0 & b_{x5} & b_{x6} \\ b_{y1} & b_{y2} & b_{y2} & b_{y1} & 0 & 0 \\ -b_{y1} l_{12} & -b_{y2} l_{12} & b_{y2} l_{12} & b_{y1} l_{12} & -b_{x5} l_{56} & -b_{x6} l_{56} \end{bmatrix} \tag{20}$$

$$b_{x5} = b_0 \sin\left[\gamma_1\left(x_6 + \frac{w}{2}\right)\right] \tag{21}$$
$$b_{x6} = -b_0 \cos\left[\gamma_1\left(x_6 + \frac{w}{2}\right)\right] \tag{22}$$
$$b_{y1} = -b_0 \cos\left[\gamma_1\left(y_1 - \frac{w}{2}\right)\right] \tag{23}$$
$$b_{y2} = b_0 \sin\left[\gamma_1\left(y_1 - \frac{w}{2}\right)\right] \tag{24}$$

where $\boldsymbol{f} = [f_{x,p}\ f_{y,p}\ T_{z,p}]^T$ is the column vector of the forces acting on the moving platen, and $\boldsymbol{i} = [i_1\ i_2\ i_3\ i_4\ i_5\ i_6]^T$ is the column vector of the currents flowing in the coils.

With the maximum electric current of 1 A flowing in each coil, the maximum resultant z-direction force generated by each set of Coils 1 and 2, Coils 3 and 4, or Coils 5 and 6 is calculated to be 4.4 N. With the stiffness of each air bearing of 17 000 N/mm, the maximum vertical displacement of the moving platen and the maximum angle errors in rotations about the y'- and x'-axes are estimated to be 0.26 μm, 6.8 μrad, and 7.4 μrad, respectively. These position errors are negligible even when fluctuating loads on the order of several newtons are vertically added into the moving platen. Thus, z_1, and therefore, b_0 are considered as constants.

III. Mechanical Design

The positioner was designed with a light-mass, compact-size, and single-moving-part platen without large extra parts for sensor mounts and air bearing supports. Delrin was chosen as the material of the frame of the moving platen because of its three advantages—high tensile strength and high hardness, light mass density, and easy machinability. Three air bearings (manufactured by Nelson Air) are used to support the moving platen against gravity and maintain a constant air gap between the coils and the aluminum plate atop the magnet matrix. Fig. 6 gives a perspective view at the bottom of the moving platen with the six coils in their locations. The coils are clamped to the moving platen at their sides by setscrews through the threaded holes in the frame body. This frame was cut by a computer-numerical-control (CNC) machine.

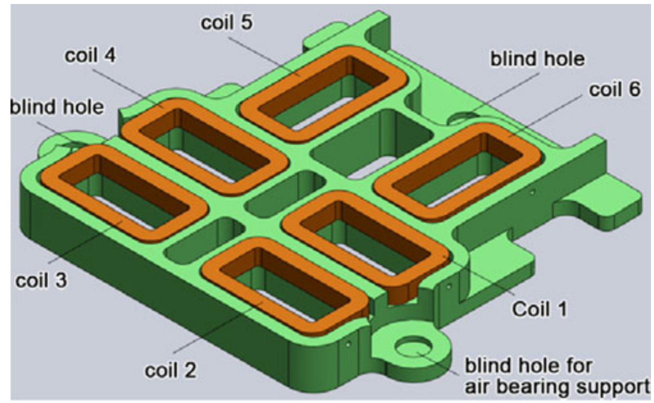

Fig. 6. Perspective view of the bottom of the Delrin frame.

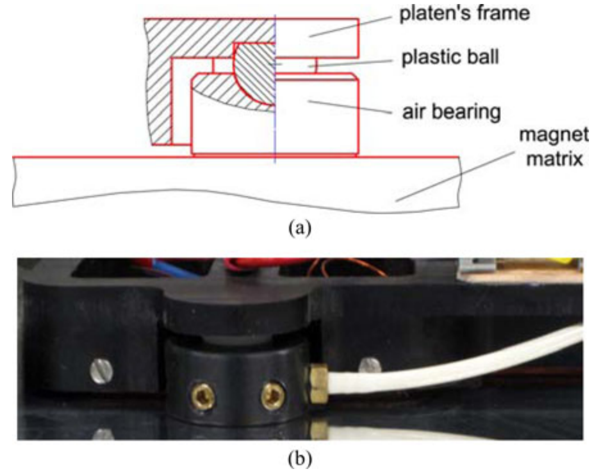

Fig. 7. (a) Part of engineering drawing and (b) photograph of the moving platen's frame with a Delrin ball and an air bearing assembled.

For the mechanical joints between the platen's frame of the platen and the air bearings, three plastic balls made of Delrin with the diameter of 12.65 mm are used. The platen's frame is designed to have three blind holes, as shown in Fig. 6, with the depth of 2.29 mm. The plastic balls are ground to be hemisphere-shape connectors. They fit directly into the frame's blind holes so that the flat surface of a connector and the bottom surface of a blind hole are in contact. The precise assembly of the platen's frame, a hemisphere-shaped connector, and an air bearing is illustrated in Fig. 7.

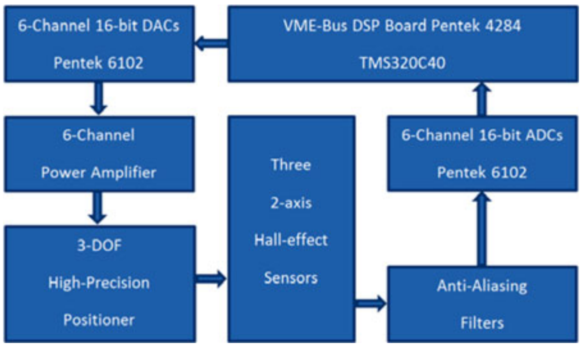

Fig. 8. Overall instrumentation block diagram.

The total mass of the moving platen, including the frame, six coils, three sensors, and connectors is $m = 0.64$ kg. The moment of inertia with respect to the principal axis z' is $I_{zz} = 0.001$ kg·m^2. As indicated in Fig. 5, the origin of the $x'y'z'$ frame is located at the center of mass of the moving platen.

IV. Instrumentation and Sensors

The overall instrumentation structure of the positioner is shown in Fig. 8. The digital-signal-processing (DSP) board that executes the real-time control routine is Pentek 4284 [15]. The DSP board is employed in a 32-bit VERSA module Eurocard (VME) system, allowing for real-time data communication with a VME computer and with external devices via the data I/O board Pentek 6102 [15] through eight channels of 16-bit analog-to-digital-converter (ADC) and eight channels of 16-bit digital-to-analog-converter (DAC). The output voltage of the DAC channels is in the range from -5 to $+5$ V. The control routines are written in C programming language with Texas Instrument's Code Composer.

Three 2-axis Hall-effect sensors (2SA-10 manufactured by Sentron AG) are used to measure the magnetic flux density above the superimposed Halbach magnet matrix. Each Hall-effect sensor can measure two orthogonal magnetic flux-density components corresponding to its two sensitive sensing directions. Since the sensors are placed so that their sensitive directions should be on the horizontal *xy* plane, the field solutions (1)–(2) and the data measured by the Hall-effect sensors are utilized to determine the position of the moving platen. Sensors 1 and 3 are to determine the moving platen's position in *x* and *y*. To determine the platen's position in small rotations about the vertical axis, Sensors 1 and 2 are used. Assuming that the position in *y* of Sensor 1 and that of Sensor 2 are, respectively, y_{s1} and y_{s2}, the position φ of the moving platen in rotation about the vertical axis is determined by

$$\varphi = \tan^{-1}\left[\frac{(y_{s2} - y_{s1})}{(5L/2)}\right]. \tag{25}$$

In Fig. 3, the locations of the Hall-effect sensors in the moving platen are given. This arrangement of the sensors is to guarantee that, along *x* and *y*, when a sensor is at a peak of the *x* or *y* magnetic flux-density component, there is another sensor placed at zero *x* or *y* magnetic flux-density component, correspondingly. This is to avoid large sensing noise from the Hall-effect sensors when they are at peaks of the sinusoidally varying magnetic flux-density components. The sensing range of 2SA-10 is from -40 to $+40$ mT, and the magnetic sensitivity is 50 V/T with the supply voltage of 5 V. At the height of 27.7 mm where the sensors are placed, the *x* and *y* magnetic flux-density components vary in the range from -16.4 to $+16.4$ mT. The sensor's bandwidth is 18 kHz [16]. The corner frequency of the antialiasing filters that we constructed, which are resistor-capacitor first-order low-pass filters, is 217 Hz. The sampling frequency of the entire digital control system is 1 kHz. Five recent samples from the sensor measurements through the ADC channels are averaged. These averaging filters function as digital low-pass filters to reduce the high-frequency sensor noise.

Six linear transconductance power-amplifier units were designed and constructed to generate six coil currents on the moving platen. The input voltages to these power amplifiers are commanded by Pentek 4284 via DAC channels of Pentek 6102. The outputs are the currents flowing in the coils. The power OP Amps (PA12A manufactured by Apex) meet the requirements of excellent linearity, high output current, and high slew rate [17]. The power amplifier's dc gain is 0.506, and its bandwidth is 6.893 kHz.

V. Controller Design

Since the air-bearing friction and stiffness are negligible in the horizontal *xy* plane, based on the Newton's second law, the moving platen's dynamics in planar motions are

$$m\frac{d^2x}{dt^2} = f_{x,p}, \quad m\frac{d^2y}{dt^2} = f_{y,p} \tag{26}$$

$$I_{zz}\frac{d^2\varphi}{dt^2} = T_{z,p}. \tag{27}$$

The relations between the resultant electromagnetic forces acting on the moving platen $f_{x,p}, f_{y,p}, T_{z,p}$, and the resultant electromagnetic forces $f_{y,12}, f_{y,34}, f_{x,56}$, respectively, acting on the set of Coils 1 and 2, Coils 3 and 4, and Coils 5 and 6 are as follows:

$$f_{x,p} = f_{x,56} \tag{28}$$

$$f_{y,p} = f_{y,12} + f_{y,34} \tag{29}$$

$$T_{z,p} = (-f_{y,12} + f_{y,34})l_{12} - f_{x,56}l_{56}. \tag{30}$$

Considering (13), (14), (17), and (18), the force–current relations are linear and position dependent with the trigonometric terms. In order to have a linear relation between the electromagnetic forces and the control efforts, the following computed currents are utilized, where u_{12}, u_{34}, and u_{56} are the control efforts

$$i_1 = -\cos\left[\gamma_1\left(y_1 - \frac{w}{2}\right)\right]u_{12} \tag{31}$$

$$i_2 = \sin\left[\gamma_1\left(y_1 - \frac{w}{2}\right)\right]u_{12} \tag{32}$$

$$i_3 = \sin\left[\gamma_1\left(y_1 - \frac{w}{2}\right)\right]u_{34} \tag{33}$$

$$i_4 = -\cos\left[\gamma_1\left(y_1 - \frac{w}{2}\right)\right] u_{34} \tag{34}$$

$$i_5 = \sin\left[\gamma_1\left(x_6 + \frac{w}{2}\right)\right] u_{56} \tag{35}$$

$$i_6 = -\cos\left[\gamma_1\left(x_6 + \frac{w}{2}\right)\right] u_{56}. \tag{36}$$

These are substituted into (13), (14), and (17), giving

$$f_{y,12} = b_0 u_{12} \tag{37}$$

$$f_{y,34} = b_0 u_{34} \tag{38}$$

$$f_{x,56} = b_0 u_{56}. \tag{39}$$

With the fast dynamics of the sensors, the antialiasing filters, and the power amplifiers being negligible, second-order digital lead-and-PI compensators are designed for the translational motions in *x* and *y*, and the rotational motion about the vertical axis. A lead compensator is designed first by the Bode plot to meet the criterion of overshoot (10%) and settling time (0.4 s). Theoretically, the mechanical dynamics of the moving platen is that of a pure mass. However, in practice, the moving platen is not a perfectly pure mass due to the aerodynamics of the air bearings and the cables connected to the moving platen. Therefore, a PI controller is added to eliminate the steady-state errors in the system's dynamics, resulting in a lead-and-PI compensator. The continuous-time lead-and-PI compensators are then converted into digital compensators. The digital lead-and-PI compensators for the translational mode and the rotational mode are, respectively,

$$C_{x,y}(z) = 9439\frac{(z-0.9790)}{(z-0.5061)}\frac{(z-0.9980)}{(z-1)} \tag{40}$$

$$C_{\varphi}(z) = 423.3\frac{(z-0.9711)}{(z-0.3900)}\frac{(z-0.9980)}{(z-1)}. \tag{41}$$

The phase margin of the translational mode is 67.7° at the crossover frequency of 29.1 Hz. The phase margin of the rotational mode is 69.3° at the crossover frequency of 26.4 Hz. The magnetic flux-density components measured by the Hall-effect sensors are converted to the positions of the moving platen, *x*, *y*, and φ in real time and then used for feedback in the control routine. At the beginning of a closed-loop-control motion, the control efforts are set to be zero. In consecutive motions, for example, the series of step responses shown in Fig. 11, the initial values of the control efforts to perform a step motion are the corresponding values of the control efforts in the steady state of the previous motion.

Taking the advantage of the 2-phase motors with 270° or 450° phase difference, a digital modified PID controller is also designed to close the control loop of the system. Here, the outputs are the B_x and B_y measured directly by the Hall-effect sensors. The reference inputs to the control system are precalculated series of magnetic flux densities corresponding to the desired positions of the moving platen. The currents flowing in the coils are as follows:

$$i_1 = I_{12}\sin(\gamma_1 u_1) \tag{42}$$

$$i_2 = I_{12}\cos(\gamma_1 u_1) \tag{43}$$

$$i_3 = I_{34}\sin(\gamma_1 u_3) \tag{44}$$

$$i_4 = I_{34}\cos(\gamma_1 u_3) \tag{45}$$

$$i_5 = I_{56}\sin(\gamma_1 u_5) \tag{46}$$

$$i_6 = I_{56}\cos(\gamma_1 u_5) \tag{47}$$

where I_{12}, I_{34}, and I_{56} are the limits of the currents flowing in the coils set to be 0.25 A. The designed controllers are expressed in the following difference-equation forms:

$$u_1[m] = u_1[m-1] + k_1(B_{y1d}[m] - B_{y1}[m]) + k_2\left(\frac{B_{y1d}[m] - B_{y1d}[m-1]}{T} - \frac{B_{y1}[m] - B_{y1}[m-1]}{T}\right) \tag{48}$$

$$u_3[m] = u_3[m-1] + k_3(B_{y2d}[m] - B_{y2}[m]) + k_4\left(\frac{B_{y2d}[m] - B_{y2d}[m-1]}{T} - \frac{B_{y2}[m] - B_{y2}[m-1]}{T}\right) \tag{49}$$

$$u_5[m] = u_5[m-1] + k_5(B_{xd}[m] - B_x[m]) + k_6\left(\frac{B_{xd}[m] - B_{xd}[m-1]}{T} - \frac{B_x[m] - B_x[m-1]}{T}\right). \tag{50}$$

Here, *T* is the sampling period of 1 ms. The control parameters k_1, k_2, k_3, k_4, k_5, and k_6 are turned to obtain the desired responses. B_{y1} and B_{y2} are the *y*-direction magnetic flux-density components measured by Sensors 1 and 2, respectively. B_{y1d} and B_{y2d} are the corresponding magnetic flux densities at the desired positions of Sensors 1 and 2 along the *y*-axis. B_x is the *x*-direction magnetic flux-density component measured by the Sensor 1 or 3. B_{xd} is the corresponding magnetic flux-density component at the desired position of the Sensor 1 or 3 along the *x*-axis.

A drawback of this modified PID controller is that the control parameters are tuned manually without a systematic approach as in the lead-and-PI compensator discussed aforesaid. However, the primary advantage is that no inverse trigonometric function is evaluated in real time to convert the magnetic flux densities measured by the Hall-effect sensors to the moving platen's position in *x* or *y*.

VI. Experimental Results

Key experimental results are given and discussed in this section to verify the working principle of the design presented in this paper. Fig. 9 shows five step responses in *x* with the step sizes of 1 mm, 500, 200, 100, and 50 μm. The overshoots and settling times are consistently 5% and 0.4 s, respectively.

Fig. 10(a) and (b) shows two ramp-input responses in *x* and *y*, respectively, with the motion range of 10 mm and the velocity of 1 mm/s. The ramp input in *x* is $x_R = -0.003 + 0.001\ (t - 39)$, being performed in the time from $t = 39$ s to $t = 49$ s. The ramp input in *y* is $y_R = -0.005 + 0.001\ (t - 29)$, being performed in the time from $t = 29$ s to $t = 39$ s. The steady-state errors in

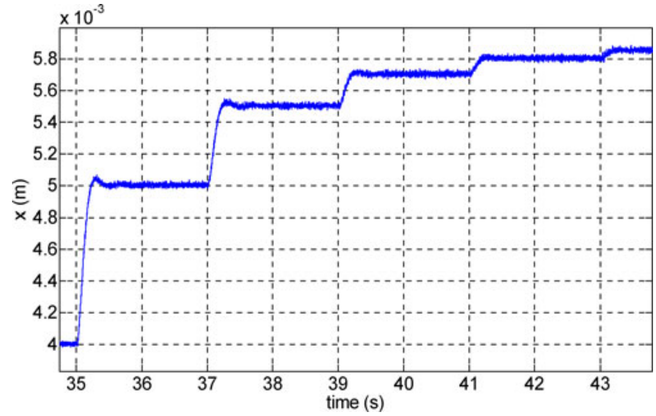

Fig. 9. Five consecutive step responses in x.

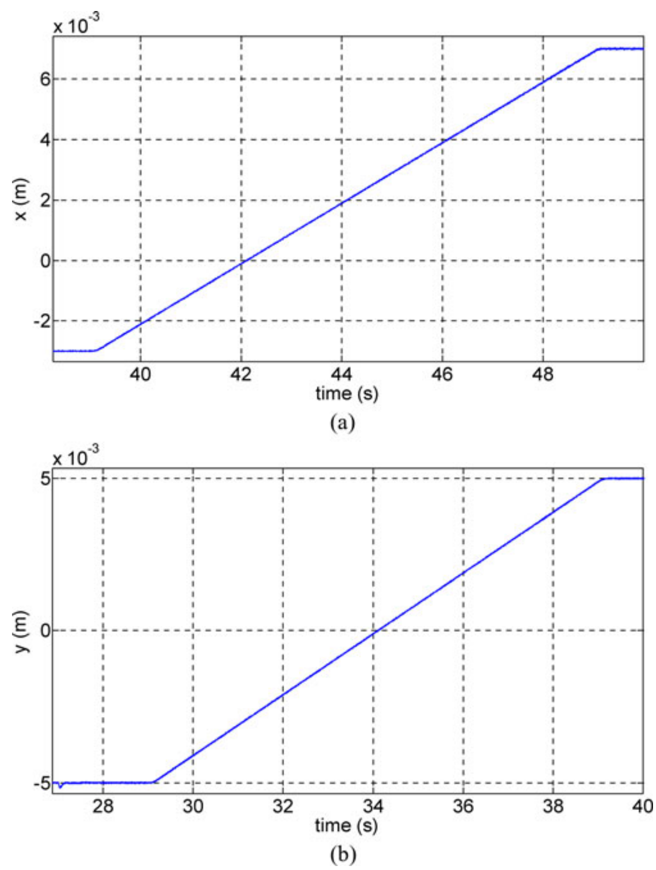

Fig. 10. Responses to the ramp inputs (a) in x and (b) in y.

both two cases are 100 μm. This means that the moving platen is not a perfectly pure mass.

Staircase responses are shown in Fig. 11 with the step size of 1 mm. The steps in Fig. 11 (a) have the time-domain specifications being consistent with those in Fig. 9 because they are implemented by the same lead-and-PI compensator. In Fig. 11(b), the responses with the modified PID controller exhibit no overshoot and the settling time of 1 s, compared to the 5% overshoot and 0.4 s settling time of those in Fig. 11(a).

In the position and velocity profiles of the translational motion shown in Fig. 12, the maximum acceleration achieved is

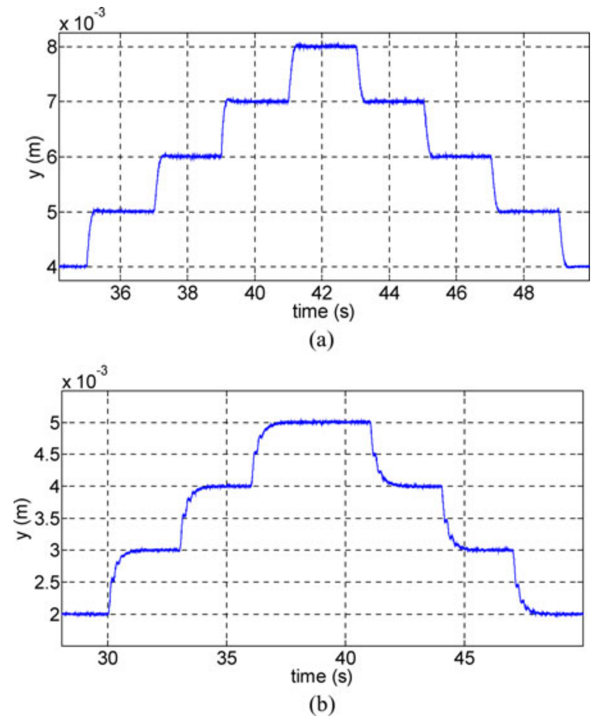

Fig. 11. Staircase responses in y by (a) lead-and-PI and (b) modified PID controllers.

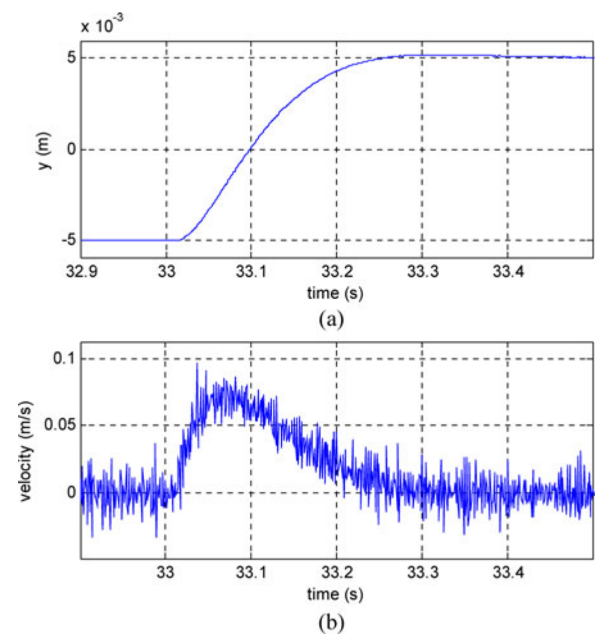

Fig. 12. (a) Position profile of a motion in y and (b) its velocity profile.

3.75 m/s^2 at the time of 33.03 s. The y-direction velocity at the time of 33.07 s is 7.5 cm/s.

The theoretical positioning resolution can be calculated as follows. The sensitive interval of the Hall-effect sensors is currently 14 mm, which corresponds to the voltage swing in the sensor output of 1.1 V. Since our 16-bit ADCs have the voltage swing of 5 V, the theoretical positioning resolution is $0.014(5/1.1)/2^{16} = 0.97\ \mu$m. The actual positioning resolution of the positioner

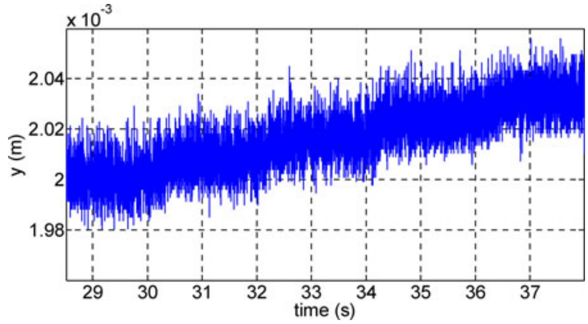

Fig. 13. Four consecutive steps of 8 μm in y.

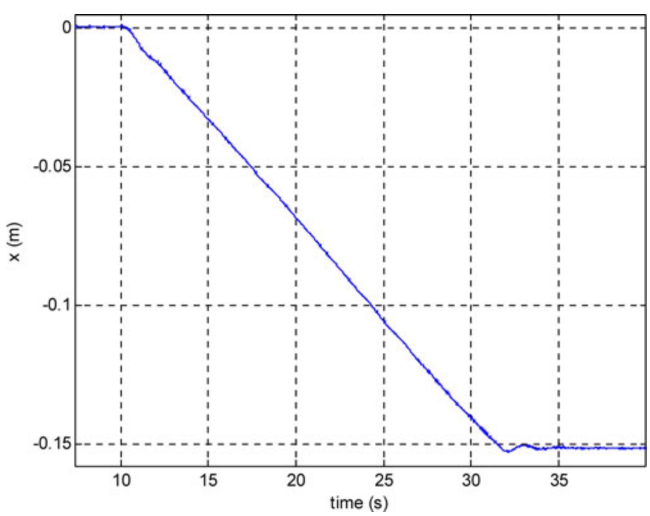

Fig. 14. Long-range translational motion of $3L = 15.24$ cm in x.

in a certain axis is determined experimentally by the positioner's smallest step size in this axis that can be seen clearly. Therefore, the sensing noise affects the positioning resolution. A larger sensing noise leads to larger step sizes that can be seen clearly, thereby degrading the positioning resolution. However, if we lower the corner frequency of the antialiasing low-pass filters in order to reduce the amplitude of the sensing noise, this will slow down the positioner's dynamic response. Thus, with the Hall-effect sensors being used, there is always a tradeoff between the positioning resolution and the response speed. In Fig. 13, there are four consecutive step responses of 8 μm, demonstrating the positioning resolution of the positioner in y. The root mean square (rms) positioning noise in x and y is 6 μm.

A long-range translational motion of $3L = 15.24$ cm in x is shown in Fig. 14 with the constant velocity of 0.70 cm/s. Fig. 15 shows a translational motion of $4L = 20.32$ cm in y with the constant velocity of 1.03 cm/s.

Fig. 16 demonstrates four consecutive rotations about the z' vertical axis to form a trapezoidal-angle profile. The constant angular velocity is 0.073 rad/s. The achieved travel range in the rotational motion about z' is 12.03°.

The average power consumption of the six-coil positioner with the lead-and-PI compensator is estimated to be 5 mW in steady state while the position of the moving platen is held precisely with the rms position noise of 6 μm. With the modified

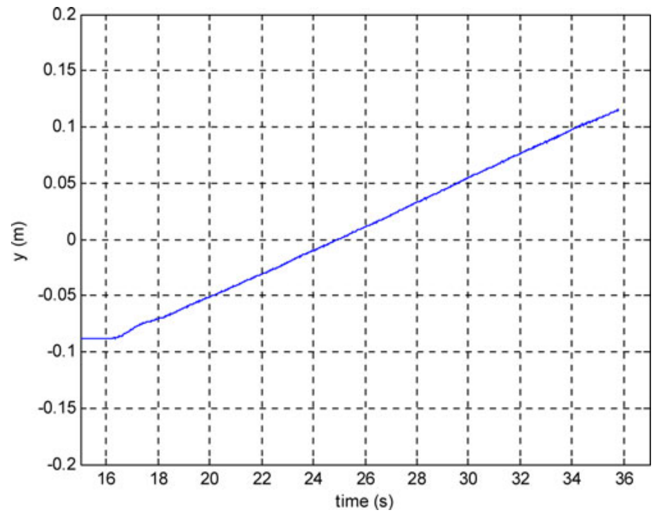

Fig. 15. Long-range translational motion of $4L = 20.32$ cm in y.

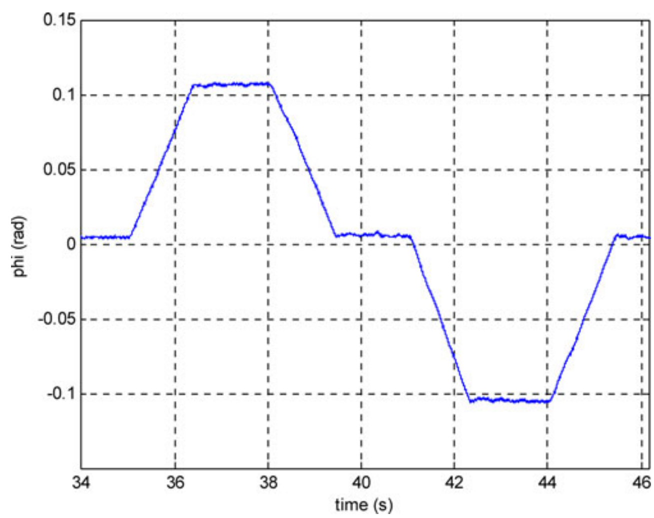

Fig. 16. Trapezoidal angle profile of rotational motions about the vertical axis.

PID controller applied and the maximum current of 0.25 A flowing in the coils, the power consumption of the six-coil platen is 370 mW, which is still reasonably small.

VII. Conclusions

In this paper, a six-coil single-moving-part positioner was designed and controlled to move over a superimposed concentrated-field magnet matrix. The actuators are three 2-phase planar motors with a 270° or 450° phase difference. The linear current-force transformation derived by volume integration allows for real-time implementation of the lead-and-PI and modified PID controllers. Representative experimental results, including step responses and ramp responses, were given to verify the commutation law and the current–force transformation of the positioner. The maximum travel ranges in x, y, and in rotation about the vertical axis are 15.24 cm, 20.32 cm, and 12.03°, respectively. The positioning resolutions are 8 μm in translation and 100 μrad in rotation. With the achieved acceleration in translational motions of 3.75 m/s^2, the overshoot of

5% and the settling time of 0.4 s in step responses, the design presented herein is highly applicable for stepping and scanning applications that require long-range precise translational motions in x and y and large rotations about the vertical axis.

REFERENCES

[1] B. A. Sawyer, "Magnetic positioning device," U.S. Patent 3 376 578, Apr. 2, 1968.

[2] W.-J. Kim, "High-precision planar magnetic levitation," Ph.D. dissertation, Massachusetts Inst. of Technol., Cambridge, Jun. 1997. [Online]. Available: http://dspace.mit.edu/handle/1721.1/10419

[3] N. Fujii and T. Kihara, "Surface induction motor for two-dimensional drive," *Electr. Eng. Jpn.*, vol. 130, no. 4, pp. 107–115, Mar. 2000.

[4] H.-S. Cho, C.-H. Im, and H.-K. Jung, "Magnetic field analysis of 2-D permanent magnet array for planar motor," *IEEE Trans. Magn.*, vol. 37, no. 5, pp. 3762–3766, Sep. 2001.

[5] H.-S. Cho and H.-K. Jung, "Analysis and design of synchronous permanent-magnet planar motors," *IEEE Trans. Energy Convers.*, vol. 17, no. 4, pp. 492–499, Dec. 2002.

[6] T.-J. Hu, "Design and control of a 6-degree-of-freedom levitated positioner with high precision," Ph.D. dissertation, Texas A&M Univ., College Station, May 2005.

[7] H. Yu and W.-J. Kim, "A compact Hall-effect-sensing 6-DOF precision positioner," *IEEE/ASME Trans. Mechatronics*, vol. 15, no. 6, pp. 982–985, Dec. 2010.

[8] Y. M. Choi and D.-G. Gweon, "A high-precision dual-servo stage using Halbach linear active magnetic bearings," *IEEE Trans. Mechatronics*, vol. 16, no. 5, pp. 925–931, Oct. 2011.

[9] S.-K. Ro and J.-K. Park, "A compact ultra-precision air bearing stage with 3-DOF planar motions using electromagnetic motors," *Int. J. Precision Eng. Manuf.*, vol. 12, no. 1, pp. 115–119, Feb. 2011.

[10] M. U. Khan, N. Bencheikh, C. Prelle, F. Lamarque, T. Beutel, and S. Buttgenbach, "A long stroke electromagnet *XY* positioning stage for micro applications," *IEEE/ASME Trans. Mechatronics*, [Online]. Available: http://ieeexplore.ieee.org, DOI: 10.1109/TMECH.2011.2142319.

[11] D. L. Trumper, W.-J. Kim, and M. E. Williams, "Design and analysis framework for linear permanent-magnet machines," *IEEE Trans. Ind. Appl.*, vol. 32, no. 2, pp. 371–379, Mar./Apr. 1996.

[12] K. Halbach, "Design of permanent multipole magnets with oriented rare earth cobalt material," *Nuclear Instrum. Methods*, vol. 169, no. 1, pp. 1–10, 1980.

[13] W.-J. Kim, N. D. Bhat, and T. Hu, "Integrated multidimensional positioner for precision manufacturing," *J. Eng. Manuf.*, vol. 218, no. 4, pp. 431–442, Apr. 2004.

[14] V. H. Nguyen, "A multi-axis compact positioner with a 6-coil platen moving over a superimposed Halbach magnet matrix," M.S. thesis, Texas A&M University, College Station, TX, May 2011. [Online]. Available after May 2012: http://hdl.handle.net/1969.1/ETD-TAMU-2011-05-9068

[15] Pentek, Inc. (2010). [Online]. Available: http://www.pentek.com

[16] Sentron AG. (2010). [Online]. Available: http://www.sentron.ch

[17] PA12A/APEX Datasheet. (2010). [Online]. Available: http://www.datasheetcatalog.com/datasheets_pdf/P/A/1/2/PA12A.shtml

Vu Huy Nguyen (S'05) received the B.S. degree in mechanical engineering from Hanoi University of Technology, Hanoi, Vietnam, in 2005, and the M.S. degree in mechanical engineering from Texas A&M University, College Station, in 2011.

He is currently a Lecturer and Researcher at the University of Transport and Communications, Hanoi. His research interests include design and control of electromechanical actuators, precision positioning, and magnetic levitation.

Won-jong Kim (S'89–M'97–SM'03) received the B.S. (*summa cum laude*) and M.S. degrees in control and instrumentation engineering from Seoul National University, Seoul, Korea, in 1989 and 1991, respectively, and the Ph.D. degree in electrical engineering and computer science from the Massachusetts Institute of Technology, Cambridge, in 1997.

Since 2000, he has been with the Department of Mechanical Engineering, Texas A&M University, College Station, where he is currently an Associate Professor. He was the inaugural holder of the Dietz Career Development Professorship II in 2007–2010. He is the holder of three U.S. patents on precision positioning systems. His current research interests include the analysis, design, and real-time control of mechatronic systems, networked control systems, and nanoscale engineering and technology.

Dr. Kim is a Technical Editor of the IEEE/ASME TRANSACTIONS ON MECHATRONICS, *ASME Journal of Dynamic Systems, Measurement and Control, International Journal of Control, Automation, and Systems*, and *Asian Journal of Control*. He is a Fellow of the ASME and a member of Pi Tau Sigma.